

# Atomic-layer Rashba-type superconductor protected by dynamic spin-momentum locking

Shunsuke Yoshizawa,<sup>1,\*</sup> Takahiro Kobayashi,<sup>2</sup> Yoshitaka Nakata,<sup>3</sup> Koichiro Yaji,<sup>4,5</sup> Kenta Yokota,<sup>6,7</sup> Fumio Komori,<sup>4</sup> Shik Shin,<sup>4,8</sup> Kazuyuki Sakamoto,<sup>3,9,10,11</sup> and Takashi Uchihashi<sup>6,7,†</sup>

<sup>1</sup>*Research Center for Advanced Measurement and Characterization, National Institute for Materials Science, 1-2-1 Sengen, Tsukuba, Ibaraki 305-0047, Japan*

<sup>2</sup>*Department of Material and Life Science, Osaka University, 2-1 Yamadaoka, Suita, Osaka 565-0871, Japan*

<sup>3</sup>*Department of Materials Science, Chiba University, 1-33 Yayoi-cho, Inage-ku, Chiba 263-8522, Japan*

<sup>4</sup>*Institute for Solid State Physics, The University of Tokyo, 5-1-5 Kashiwanoha, Kashiwa, Chiba 277-8581, Japan*

<sup>5</sup>*Present address: Research Center for Advanced Measurement and Characterization, National Institute for Materials Science, 1-2-1 Sengen, Tsukuba, Ibaraki 305-0047, Japan*

<sup>6</sup>*International Center for Materials Nanoarchitectonics (WPI-MANA), National Institute for Materials Science, 1-1 Namiki, Tsukuba, Ibaraki 305-0044, Japan*

<sup>7</sup>*Department of Condensed Matter Physics, Graduate School of Science, Hokkaido University, Kita 8, Nishi 5, Kita-ku, Sapporo, Hokkaido 060-0808, Japan*

<sup>8</sup>*Office of University Professor, The University of Tokyo, Kashiwa, Chiba, Japan*

<sup>9</sup>*Center for Spintronics Research Network, Graduate School of Engineering Science, Osaka University, Toyonaka, Osaka, Japan*

<sup>10</sup>*Department of Applied Physics, Osaka University, 2-1 Yamadaoka, Suita, Osaka 565-0871, Japan*

<sup>11</sup>*Molecular Chirality Research Center, Chiba University, 1-33 Yayoi-cho, Inage-ku, Chiba 263-8522, Japan*

## Abstract

Spin-momentum locking is essential to the spin-split Fermi surfaces of inversion-symmetry broken materials, which are caused by either Rashba-type or Zeeman-type spin-orbit coupling (SOC). While the effect of Zeeman-type SOC on superconductivity has experimentally been shown recently, that of Rashba-type SOC remains elusive. Here we report on convincing evidence for the critical role of the spin-momentum locking on crystalline atomic-layer superconductors on surfaces, for which the presence of the Rashba-type SOC is demonstrated. In-situ electron transport measurements reveal that in-plane upper critical magnetic field is anomalously enhanced, reaching approximately three times the Pauli limit at  $T = 0$ . Our quantitative analysis clarifies that dynamic spin-momentum locking, a mechanism where spin is forced to flip at every elastic electron scattering, suppresses the Cooper pair-breaking parameter by orders of magnitude and thereby protects superconductivity. The present result provides a new insight into how superconductivity can survive the detrimental effects of strong magnetic fields and exchange interactions.

---

\* YOSHIZAWA.Shunsuke@nims.go.jp

† UCHIHASHI.Takashi@nims.go.jp

## INTRODUCTION

The breaking of the out-of-plane or in-plane inversion symmetry in two-dimensional (2D) systems gives rise to Rashba-type or Zeeman-type spin-orbit coupling (SOC), respectively, which plays important roles in spintronics, valleytronics, optoelectronics and superconductivity [1–5]. Both types of SOC cause the Fermi surface to be spin-split and the spin-momentum relation to be locked, but the spin polarisation in the momentum space is distinctively different; Rashba-type SOC forces the spins to be polarised in the in-plane direction while Zeeman-type SOC in the out-of-plane direction (Fig. 1a and 1b) [1, 2]. These unique spin structures have notable implications in terms of superconductivity under strong magnetic fields [6–13].

Suppose the magnetic field is applied to a 2D superconductor precisely in the in-plane direction. Since electron orbitals are barely affected in this configuration, Cooper pairs are destroyed mainly due to the field-induced parallel alignment of the electron spins, which otherwise form an anti-parallel spin-singlet state. This mechanism is called paramagnetic pair breaking, and the upper critical magnetic field  $B_{c2\parallel}$  determined by this effect is called the Pauli limit  $B_{\text{Pauli}}$  [14, 15]. In the presence of Zeeman-type SOC, the spins are hardly tilted in the field direction because they are statically locked in the out-of-plane direction. This suppresses the paramagnetic pair breaking effect and substantially enhances  $B_{c2\parallel}$  over  $B_{\text{Pauli}}$  [8, 9]. By contrast, the in-plane spin-momentum locking due to Rashba-type SOC can enhance  $B_{c2\parallel}$  only by a factor of  $\sqrt{2}$  because of a significant deformation of the Fermi surfaces due to the locking [6]. Nevertheless, Rashba-type SOC may also strongly enhance  $B_{c2\parallel}$  if a dynamic electron scattering process is involved. In this case, because of the spin-momentum locking, the spin is forced to flip at every momentum change accompanied by elastic scattering (Fig. 1c). The mechanism, referred to as dynamic spin-momentum locking here, should cause frequent spin scatterings while preserving the time-reversal symmetry. This enhances  $B_{c2\parallel}$  through the suppression of paramagnetic pair-breaking effect even in crystalline systems in an analogous manner as the conventional spin-orbit scattering does in disordered systems. Although such an effect was suggested by Nam et al. for Pb thin films, it was considered dominated by the orbital pair-breaking and hence has remained elusive [10]. Furthermore, the presence of the Rashba-type SOC itself was an assumption, and the material may include Zeeman-type SOC [11]. Experimentally resolving this problem requires one to confirm the exclusive presence of the Rashba-type SOC in a relevant system. It is also important to investigate its superconducting properties under a controlled environment to avoid any extrinsic effects.

In the present study, we adopt a crystalline In atomic-layer on a Si(111) surface [Si(111)-( $\sqrt{7} \times \sqrt{3}$ )-In] to fulfil this requirement. Clear Fermi surface splitting and in-plane spin polarisation are demonstrated by angle-resolved photoemission spectroscopy (ARPES) and density functional theory (DFT) calculations, confirming the exclusive presence of the Rashba-type SOC. In-situ electron transport measurements under ultrahigh vacuum (UHV) environment reveal that  $B_{c2\parallel}$  is anomalously enhanced over the Pauli limit  $B_{\text{Pauli}}$ . The enhancement factor defined by  $B_{c2\parallel}/B_{\text{Pauli}}$  reaches  $\sim 3$  and exceeds the factor of  $\sqrt{2}$  expected for the static locking effect of the Rashba-type SOC. Our quantitative data analysis clarifies that the paramagnetic pair-breaking parameter  $\alpha_P$  is strongly suppressed by orders of magnitudes from the value estimated for the conventional spin-orbit scattering. The spin scattering times  $\tau_s$  directly related to  $\alpha_P$  are in satisfactory agreement with the electron elastic scattering times  $\tau_{\text{el}}$ , proving the idea of spin flipping at every momentum change. These results provide compelling evidence that this 2D superconductor with Rashba-type SOC is protected by dynamic spin-momentum locking.

## RESULTS

### Rashba-type SOC revealed by ARPES and DFT

The Si(111)-( $\sqrt{7} \times \sqrt{3}$ )-In (referred to as  $\sqrt{7} \times \sqrt{3}$ -In here) consists of a uniform In bilayer covering the Si(111)- $1 \times 1$  surface with a periodicity of  $\sqrt{7} \times \sqrt{3}$  (Fig. 2a) [16, 17], and superconductivity occurs below 3 K [18, 19]. The breaking of the out-of-plane inversion symmetry due to the presence of the Si surface leads to the Rashba-type SOC as described below, as reported for other atomic-layer crystals on surfaces [20–23]. The material has highly dispersed electronic bands and simple chemical composition without magnetic or heavy elements [24], which allows us to neglect complex correlation effects. Despite these ideal features, studying superconducting properties of  $\sqrt{7} \times \sqrt{3}$ -In is challenging because the susceptibility to foreign molecules and surface defects prohibits air exposure and the usage of conventional cryogenic and high-magnetic-field systems [25, 26]. In this study, all experiments, including the transport measurements, were performed in UHV to eliminate the possibility of sample degradation (see Materials and Methods).

The details of the electronic structures and the presence of Rashba-type SOC are clarified through ARPES measurements and DFT calculations. Figure 2c shows the photoelectron intensity map at the Fermi energy ( $E_F$ ) measured over the momentum-space region depicted in Fig.

2b. While the result is consistent with the previous studies [16, 24], it clearly resolves the splitting of the Fermi surfaces for the first time, which is particularly conspicuous on the “arc” and “butterfly-wing” portions (see the pairs of arrows). This finding was fully reproduced by our DFT calculations. The computed Fermi surface structure is essentially identical to the ARPES data (Fig. 3a). While the magnitude of the energy splitting at  $E_F$  ( $\Delta_R$ ) is small along the high-symmetry lines (Y– $\Gamma$ –X), it is larger at the butterfly-wing along the P–Q line (Fig. 3f). Figure 3c shows that the distribution of  $\Delta_R$  exhibits a peak around 15–20 meV and ranges up to 90 meV. The DFT calculations also confirm that these Fermi surfaces are indeed spin-polarised. As indicated by the arrows in Fig. 3a, the spins are oriented in the in-plane directions, as expected from Rashba-type SOC. The effect of Zeeman-type SOC is negligible, judging from the fact that the out-of-plane components of spins are nearly absent (Fig. 3d). This point will be discussed later in detail. Interestingly, the azimuthal orientation of the spins on the butterfly-wing features deviates from the helical spin texture characteristic of the standard Rashba-type SOC. This in-plane spin texture does not affect the conclusion of the present study, and its microscopic origin will be discussed elsewhere [27]. We also mention the presence of a large anisotropy in the Fermi velocity  $\mathbf{v}_F$ , which was computed as the gradient of band dispersion (Fig. 3b). The histogram in Fig. 3e shows that  $|\mathbf{v}_F|$  ranges from  $2 \times 10^5$  to  $1.5 \times 10^6$  m·s<sup>−1</sup>. The detailed band structure information obtained here will be used later.

### **Robust superconductivity in in-plane magnetic fields**

Six  $\sqrt{7} \times \sqrt{3}$ -In samples were prepared for electron transport experiments. In addition to three nominally flat Si(111) surfaces (Flat#1/#2/#3), we used three vicinal surfaces (Vicinal#1/#2 with a miscut angle of 0.5° and Vicinal#3 with a miscut angle of 1.1°) to control the density of scattering sources. These sample surfaces consisted of atomically flat terraces separated by steps, as observed by scanning tunnelling microscopy (STM) (Fig. 4a: Flat#1, Fig. 4b: Vicinal#1). The low-energy electron diffraction (LEED) patterns of Flat#1 and Vicinal#1 confirmed the exclusive presence of  $\sqrt{7} \times \sqrt{3}$  structures with multi- and single-domains, respectively (Insets of Figs. 4a and 4b). Figure 4c shows the temperature ( $T$ ) dependence of sheet resistance ( $R_{\text{sheet}}$ ) recorded at zero magnetic field. The curves of the other four samples are available in Supplementary Figure 1. All of the samples exhibit sharp superconducting transitions at  $T_{c0}$ , while precursors due to the 2D fluctuation effects are evident at  $T > T_{c0}$  [28]. Here  $T_{c0}$  is defined as the Bardeen-Cooper-Schrieffer (BCS) mean-field critical temperature, which was determined by fitting to an empirical

formula [29] (see Supplementary Note 1). The same fitting procedure also gives normal sheet resistance  $R_n$  in the absence of the 2D fluctuation effects. The obtained parameters for  $T_{c0}$  and  $R_n$  are presented in Table 1. The small  $R_n$  of 36-90  $\Omega$  reflects the high crystallinity of the samples. These values are comparable to those reported for transition-metal dichalcogenide samples used in the studies of Zeeman-type SOC [8, 9].

We now focus on the effects of strong magnetic fields on superconductivity of  $\sqrt{7} \times \sqrt{3}$ -In. Figure 5a shows the temperature dependence of sheet resistance  $R_{\text{sheet}}$  of Vicinal#1 measured under magnetic fields, which were applied precisely in the in-plane direction. The data of the other samples are presented in Supplementary Figure 2. While slight shifts and broadenings of the resistive transition were detected, superconductivity persisted even at the maximum magnetic field of  $B = 5$  T. Figure 5c shows the magnetic field dependence of  $T_c$  of all six samples, where  $T_c$  is determined from  $T$  at which  $R_{\text{sheet}}$  decreases to half of  $R_n$ . The data show that the lowering of  $T_c$  as a function of  $B$  is quadratic and reaches 23% of  $T_{c0}$  at 8.25 T for Flat#3. By contrast, for out-of-plane magnetic fields, the superconducting transition was rapidly suppressed and disappeared above  $B = 0.5$  T (Fig. 5b). The lowering of  $T_c$  as a function of  $B$  is linear (Fig. 5d). Our detailed analysis for out-of-plane upper critical field  $B_{c2\perp}$  shows that the observed rapid quenching of superconductivity is due to penetration of vortices, i.e. to orbital pair-breaking effect (see Supplementary Figure 3 and Supplementary Note 2). The robust superconductivity against the in-plane fields, in contrast, indicates that the pair-breaking is not caused by the orbital effect but rather by the paramagnetic effect as expected. For the present superconductor with  $T_{c0} = 2.97\text{--}3.14$  K, the Pauli limit  $B_{\text{Pauli}}$  is equal to 5.5–5.8 T from the relation  $B_{\text{Pauli}} = 1.86 (\text{T} \cdot \text{K}^{-1}) T_{c0}$  [14, 15]. Since the observed  $B_{c2\parallel}$  apparently exceeds this limit as  $T \rightarrow 0$ , the paramagnetic pair breaking effect must be substantially suppressed.

### **Paramagnetically limited upper critical field**

It is widely known that spin scattering is induced occasionally at an elastic electron scattering event by the atomistic SOC. In the presence of this conventional spin-orbit scattering, Cooper pairs are no longer exact spin-singlet states. It induces a finite spin susceptibility in the system and lowers the Zeeman energy gain acquired by breaking a Cooper pair under a magnetic field, thus suppressing the paramagnetic pair-breaking effects [30]. Here we assume this mechanism and, without taking account of the Rashba-type SOC, analyse the magnetic field effects on supercon-

ductivity in terms of pair-breaking parameters. The dependence of  $T_c$  on magnetic field  $\mathbf{B}$  can be described using a universal function given by

$$\ln\left(\frac{T_c}{T_{c0}}\right) = \psi\left(\frac{1}{2}\right) - \psi\left(\frac{1}{2} + \frac{\alpha(\mathbf{B})}{2\pi k_B T_c}\right), \quad (1)$$

where  $\psi$  is the digamma function, and  $\alpha(\mathbf{B})$  denotes field-dependent pair-breaking parameter [31].  $\alpha(\mathbf{B})$  is the sum of three contributions:  $\alpha_{O\perp}$  and  $\alpha_{O\parallel}$  representing the orbital effects due to out-of-plane ( $B_{\perp}$ ) and in-plane ( $B_{\parallel}$ ) fields and  $\alpha_P$  the paramagnetic effect due to the total field  $|\mathbf{B}|$  in the presence of frequent spin scatterings. It is given by the equation

$$\alpha(\mathbf{B}) = \alpha_{O\perp} + \alpha_{O\parallel} + \alpha_P \quad (2)$$

$$= c_{O\perp} B_{\perp} + c_{O\parallel} B_{\parallel}^2 + c_P |\mathbf{B}|^2, \quad (3)$$

where  $c_{O\perp}$ ,  $c_{O\parallel}$  and  $c_P$  are coefficients for individual contributions [32]. This form of the pair-breaking parameter is closely related to the Klemm-Luther-Beasley (KLB) model proposed for 2D superconductors with conventional spin-orbit scattering [33, 34].

In the present study, the addition of the  $\alpha_{O\parallel}$  term allows us to account for the orbital effect within the superconducting layer under the in-plane magnetic field, which is not included in the KLB model. This effect played a crucial role in few-layer Pb films studied previously [10]. For the in-plane configuration,  $B_{\perp} \simeq \theta_e |\mathbf{B}|$  and  $B_{\parallel} \simeq |\mathbf{B}|$ , where  $\theta_e$  is the angular error. All coefficients were determined by fitting Eq. (1) to the experimental data in Figs. 5c and 5d, and the results are listed in Table 1 (for details, see Materials and Methods). From the values of  $c_{O\perp}$ ,  $c_{O\parallel}$ ,  $c_P$ , we conclude  $\alpha_{O\perp}, \alpha_{O\parallel} \ll \alpha_P$  in the in-plane configuration, meaning that the pair breaking is dominated by the paramagnetic effect. This is distinct from the finding by Nam et al. that the orbital effect is the primary pair breaking mechanism for 5–13 Pb monolayers on the Si(111) surface [10]. Figure 5e plots  $B_{c2\parallel}/B_{\text{Pauli}}$  and  $B_{c2\perp}/B_{\text{Pauli}}$  as a function of  $T_c/T_{c0}$ , along with their extrapolations down to  $T = 0$  calculated with the universal function of Eq. (1).  $B_{c2\parallel}/B_{\text{Pauli}}$  is found to reach  $\sim 3$  at  $T = 0$ . We note that this enhancement factor exceeds the value of  $\sqrt{2}$ , which is expected for the static effect of Rashba-type spin momentum locking. This claim is directly evidenced by the maximum value of  $B_{c2\parallel}/B_{\text{Pauli}} = 1.43$  obtained for Flat#3.

### Spin flipping rate enhanced by dynamic spin-momentum locking

The strong enhancement of  $B_{c2\parallel}$  observed above is actually not attributed to the atomistic SOC, but to the Rashba-type SOC as explained in the following. We first estimate elastic scattering time

$\tau_{\text{el}}$  from the normal-state sheet resistance  $R_{\text{n}}$ . The calculation was carried out by explicitly considering the anisotropy of Fermi velocity  $\mathbf{v}_{\text{F}}$  computed above (Figs. 3c and 3d) and by employing the Boltzmann theory under relaxation approximation [35]. The sheet conductance is given by

$$\sigma_{\mu\mu} = \tau_{\text{el}} I_{\mu\mu} \quad (4)$$

with

$$I_{\mu\mu} \equiv \frac{e^2}{(2\pi)^2 \hbar} \int_{\text{FS}} dk \frac{v_{\text{F}\mu}(\mathbf{k})^2}{|\mathbf{v}_{\text{F}}(\mathbf{k})|}, \quad (5)$$

where  $v_{\text{F}\mu}$  ( $\mu = x$  or  $y$ ) is the  $\mu$  component of  $\mathbf{v}_{\text{F}}$ . The integral was taken over all the spin-split Fermi surfaces, yielding  $I_{xx} = 3.9 \times 10^{-4} \Omega^{-1} \text{fs}^{-1}$  and  $I_{yy} = 4.5 \times 10^{-4} \Omega^{-1} \text{fs}^{-1}$ .  $\tau_{\text{el}}$  was evaluated from  $R_{\text{n}}^{-1} = (\sigma_{xx} + \sigma_{yy})/2$  for multi-domain flat samples (Flat#1/#2/#3) and from  $R_{\text{n}}^{-1} = \sigma_{xx}$  for single-domain vicinal samples (Vicinal#1/#2/#3). This gives  $\tau_{\text{el}} = 71.7, 53.3, 44.9 \text{ fs}$  for Flat#1/#2/#3 and  $\tau_{\text{el}} = 28.6, 39.2, 31.4 \text{ fs}$  for Vicinal#1/#2/#3, respectively (Table 1). We then estimate the spin scattering time  $\tau_{\text{s}}$  from the coefficient  $c_{\text{P}}$  for paramagnetic pair breaking effect.  $\tau_{\text{s}}$  is calculated with an equation

$$c_{\text{P}} = \frac{3\tau_{\text{s}}\mu_{\text{B}}^2}{2\hbar}, \quad (6)$$

where  $\mu_{\text{B}}$  is the Bohr magneton and  $\hbar$  the reduced Plank constant [36]. This gives  $\tau_{\text{s}} = 86 \pm 12, 52 \pm 14, 33 \pm 18 \text{ fs}$  for Flat#1/#2/#3, and  $\tau_{\text{s}} = 69 \pm 12, 70 \pm 12, 57 \pm 12 \text{ fs}$  for Vicinal#1/#2/#3 (see Table 1). These results lead to  $\tau_{\text{el}}/\tau_{\text{s}} \simeq 0.5 - 1$ . Nevertheless, if only the conventional spin-orbit scattering is considered,  $\tau_{\text{s}}$  should be much larger than the  $\tau_{\text{el}}$ . In this case, the ratio  $\tau_{\text{el}}/\tau_{\text{s}}$  should be on the order of  $(Z\alpha)^4$ , where  $Z$  is the atomic number and  $\alpha$  is the fine structure constant [30]. For In ( $Z = 49$ ),  $\tau_{\text{el}}/\tau_{\text{s}} \sim 1/60$ . An experimental study reported an even smaller  $\tau_{\text{el}}/\tau_{\text{s}}$  of about  $10^{-3}$  for thin In films [37]. Therefore, the spin-orbit scattering that occurs in the absence of the Rashba-type SOC cannot account for our result. In contrast, if the Rashba-type SOC is considered, it can be reasonably explained based on the concept of dynamic spin-momentum locking; namely, every elastic scattering should contribute a spin flipping and  $\tau_{\text{el}}/\tau_{\text{s}}$  approaches unity. The decrease in  $\tau_{\text{s}}$  together with Eq. (3) and Eq. (6) means the paramagnetic pair breaking parameter  $\alpha_{\text{P}}$  is suppressed by orders of magnitude from the value expected for the conventional spin-orbit scattering.

Remarkably, for the flat samples,  $\tau_{\text{s}}$  falls equal to  $\tau_{\text{el}}$  within the experimental error. By contrast,  $\tau_{\text{s}}$  is larger than  $\tau_{\text{el}}$  by a factor of two for the vicinal samples. This can be reasonably explained by an energy broadening caused by electron elastic scattering,  $\hbar/\tau_{\text{el}}$ . For vicinal samples,  $\hbar/\tau_{\text{el}} = 16\text{--}24 \text{ meV}$  is comparable to the peak energy in the distribution of  $\Delta_{\text{R}}$  (see Fig. 3b). This energy



broadening degrades the spin polarisation at a large portion of the Fermi surface and partially unlocks the spin-momentum relation, resulting in a recovery of spin scattering time  $\tau_s$ . For flat samples,  $\hbar/\tau_{el} = 9\text{--}14\text{ meV} < \Delta_R$ , meaning that the spin texture of the energy bands remains intact for the whole Fermi surface. This argument further supports our conclusion on the critical role of the dynamic effect of the Rashba-type SOC.

Finally, we note that the static spin-momentum locking due to the Rashba-type SOC can enhance the in-plane critical field  $B_{c2\parallel}$  by a factor of  $\sqrt{2}$  from the Pauli limit. This effect is likely to be weakened by electron scattering and mixing between different spin states, but here we estimate the upper limit of error in spin scattering time  $\tau_s$  (for a detailed discussion, see Supplementary Note 3). When it is taken into account as an effective magnetic field  $B_{eff} = (1/\sqrt{2})B$ , the value of  $\tau_s$  obtained above is doubled, leading to  $\tau_{el}/\tau_s = 0.25\text{--}0.5$ . These values are still much higher than  $1/60\text{--}1/1000$  expected from the atomistic spin-orbit scattering mechanism. Therefore, the result is not attributable only to the conventional mechanism, and our conclusion remains the same.

## DISCUSSION

Here we discuss the consistency with the theoretical studies of Rashba-type superconductors with non-magnetic impurities [10, 38–40]. These studies predict that upper critical field increases with the decrease in elastic scattering time  $\tau_{el}$ . In 2D, the enhancement factor corresponds to a pair-breaking parameter  $\alpha = (2\mu_B^2\tau_{el}/\hbar)B^2$  in the limit of strong SOC ( $\hbar/\tau_{el} \ll \Delta_R$ ) [10]. This expression is equivalent to Eq. (6) if  $\tau_s$  is replaced by  $(4/3)\tau_{el}$ . The agreement allows us to interpret the above theoretical result in terms of dynamic spin-momentum locking. Theories also claim that the ground state of a 2D superconductor with Rashba-type SOC has a helical state with a spatially modulated order parameter [38–40]. The formation of the helical state may increase  $B_{c2\parallel}$ , and a previous study on a quench-condensed monolayer Pb film attributed their observation of giant  $B_{c2\parallel}$  to this effect [7]. However, the enhancement factor is only in the order of  $\sim(\Delta_R/E_F)^2$  and is usually negligible because  $\Delta_R \ll E_F$  [40]. Therefore, the observed large  $B_{c2\parallel}$  in the present and previous studies are not attributable to the formation of the helical state.

Another issue to be discussed is the possible effect of a finite Zeeman-type SOC, which is suggested from the non-zero out-of-plane spin polarizations shown in Fig. 3d. From the spin polarization direction calculated as a function of energy splitting, one sees that the spins align in the in-plane directions for the most of energy regions (Supplementary Figure 6). The spins tend

to tilt toward the out-of-plane direction below 30 meV, but the off-angle is about  $45^\circ$  at most. Namely, there is no region where the Zeeman-type SOC is dominant. This non-dominant Zeeman SOC confined to small area of the Fermi surface can barely enhance  $B_{c2\parallel}$  because the enhancement factor is determined by an average over the whole Fermi surface [41]. If the dynamics of spins is considered, the effect of the Zeeman-type SOC can be suppressed even more. Thus, we conclude that the Zeeman-type SOC plays only a minor role in the present system. For more discussions, see Supplementary Note 4.

The present result has significant implications in terms of robustness of a superconductor with the Rashba-type SOC in general under a strong magnetic field as well as in the proximity of a ferromagnet. The presence of a strong exchange interaction at the interface with a ferromagnet usually leads to the destruction of superconductivity to the depth of the coherence length. However, since the destruction of superconductivity by exchange interaction is caused by the same paramagnetic pair-breaking effect [32], the dynamic spin-momentum locking revealed here may help superconductivity to persist even in this situation. This makes realistic the coexistence of a 2D superconductor and a ferromagnet at atomic scales, which has been proposed to realise emergent phenomena such as chiral topological superconductivity[42–44]. The new insight into the spin-momentum locking obtained in the present study will form the basis of such an unexplored realm of research.

## METHODS

### ARPES

The high-resolution ARPES experiment was conducted in a UHV environment with a base pressure better than  $1 \times 10^{-8}$  Pa. The substrate was cut from an n-type (resistivity  $\rho < 0.001 \Omega \text{ cm}$ ) vicinal Si(111) wafer with a miscut angle of  $0.5^\circ$  in the  $[\bar{1}\bar{1}2]$  direction. The  $\sqrt{7} \times \sqrt{3}$ -In surface was prepared by thermal deposition of In onto a clean Si(111)- $7 \times 7$  surface followed by annealing at 600 K for 2 min. The sample quality was confirmed from the sharp spots with low background intensity in the LEED patterns. The photoelectrons were excited by a vacuum-ultraviolet laser ( $h\nu = 6.994 \text{ eV}$ ) and were collected by a hemispherical photoelectron analyser [45]. The sample temperature was maintained at 35 K during the ARPES measurement. The energy and momentum resolutions were 3 meV and  $1.4 \times 10^{-3} \text{ \AA}^{-1}$ , respectively.

## DFT

The DFT calculations were performed using the Quantum ESPRESSO package [46]. We employed the augmented plane wave method and used the local density approximation (LDA) for the exchange correlation. The crystal structure of  $\sqrt{7} \times \sqrt{3}$ -In was modelled by a repeated slab consisting of an In bilayer, six Si bilayers, a H layer for termination, and a vacuum region of thickness 3 nm. We used a cutoff energy of 680 eV for the wave functions and a  $6 \times 8 \times 1$   $k$ -point mesh for the Brillouin zone. The geometry optimisation was performed without the SOC until all components of all forces became less than  $2.6 \times 10^{-3}$  eV·Å<sup>-1</sup>. Based on the optimised structure, we performed band calculations that included the SOC. To check the reproducibility of our result, we carried out the same calculation from scratch using another DFT package OpenMX[47, 48]. The result by OpenMX is essentially the same as the one by Quantum ESPRESSO (See Supplementary Figures 5 and 6, as well as Supplementary Note 5).

## Electron transport

For transport experiments, six samples were grown on substrates cut from Si(111) wafers (3 mm  $\times$  8 mm  $\times$  0.38 mm) with miscut angles of 0° (Flat#1, Flat#2, and Flat#3), 0.5° (Vicinal#1 and Vicinal#2), and 1.1° (Vicinal#3) in the  $[\bar{1}\bar{1}2]$  direction. The non-doped wafers ( $\rho \gtrsim 1000$  Ω cm) were chosen so that the electron conduction in bulk can be ignored at low temperatures. The  $\sqrt{7} \times \sqrt{3}$ -In surface was prepared under the UHV condition (base pressure  $1 \times 10^{-8}$  Pa) by depositing In onto a clean Si(111)- $7 \times 7$  surface followed by annealing at 600 K for 10 s. The samples were then characterized by LEED and STM. The current path was defined by Ar<sup>+</sup> sputtering using a shadow mask technique [19, 29]. Electric contact was made at room temperature by mildly pressing four Au-plated spring probes. The samples were then cooled down to ~0.9 K or to ~0.4 K by pumping condensed <sup>4</sup>He or <sup>3</sup>He with a charcoal sorption pump. The magnetic fields were applied with a superconducting solenoid magnet. The maximum field was 5 T in the experiment of Flat#1/#2 and Vicinal#1/#2/#3 and was 8.25 T in the experiment of Flat#3. The sample was rotated in-situ to tune the angle of the magnetic fields with respect to the sample. The parallel field alignment was judged within an accuracy better than 0.1° from the minimum of sample resistance measured at a constant temperature near the  $T_c$ . The sample temperature was measured with a Cernox thermometer calibrated in magnetic fields. The DC resistance of

the samples was measured using a nanovoltmeter (Keithley 2182A) with a bias current of 1  $\mu\text{A}$  generated by a source meter (Keithley 2401).

### Fitting analysis of pair-breaking effects

In the following, we denote  $|\mathbf{B}|$  as  $B$  for simplicity. The pair-breaking parameters for orbital effects are given by

$$\alpha_{\text{O}\parallel} = \frac{De^2\delta^2 B_{\parallel}^2}{6\hbar} \equiv c_{\text{O}\parallel} B_{\parallel}^2 \quad (7)$$

for the in-plane component, and

$$\alpha_{\text{O}\perp} = DeB_{\perp} \equiv c_{\text{O}\perp} B_{\perp} \quad (8)$$

for the out-of-plane component of the magnetic fields [32]. Here,  $D$  is the diffusion coefficient, and  $\delta$  represents the thickness of the superconducting layer. We assume  $\delta = 4.5 \text{ \AA}$ , which is twice the height difference between the upper and lower atoms in the In bilayer (Fig. 1a). Note that  $c_{\text{O}\parallel}$  is related to  $c_{\text{O}\perp}$  as follows:

$$c_{\text{O}\parallel} = \frac{\pi\delta^2}{6\Phi_0} c_{\text{O}\perp}. \quad (9)$$

The pair-breaking parameter for the paramagnetic effect in the presence of spin-orbit scattering is given by

$$\alpha_{\text{P}} = \frac{3\mu_{\text{B}}^2 B^2 \tau_{\text{so}}}{2\hbar} \equiv c_{\text{P}} B^2. \quad (10)$$

The total pair-breaking parameter is the sum of all contributions and is given by Eq. (3). Near  $T_{\text{c0}}$ , the universal function Eq. (1) has an approximate form given by,

$$T_{\text{c}} = T_{\text{c0}} - \frac{\pi\alpha}{4k_{\text{B}}}. \quad (11)$$

For the in-plane field, we take  $B_{\perp} \simeq \theta_{\text{e}} B$  and  $B_{\parallel} \simeq B$  in Eq. (3). The explicit form of the fitting function becomes,

$$T_{\text{c}} = T_{\text{c0}} - \frac{\pi}{4k_{\text{B}}} c_{\text{O}\perp} \theta_{\text{e}} B - \frac{\pi}{4k_{\text{B}}} (c_{\text{O}\parallel} + c_{\text{P}}) B^2. \quad (12)$$

For the out-of-plane field, we take  $B_{\perp} \simeq B$  and assumed that  $c_{\text{O}\parallel} B_{\parallel}^2, c_{\text{P}} B_{\parallel}^2 \ll c_{\text{O}\perp} B_{\perp}$ . The fitting function becomes,

$$T_{\text{c}} = T_{\text{c0}} - \frac{\pi}{4k_{\text{B}}} c_{\text{O}\perp} B. \quad (13)$$

These functions, (12) and (13), are fitted to the  $T_{\text{c}}$  curves in Figs. 5b and 5d, respectively.  $c_{\text{O}\parallel}$  and  $c_{\text{P}}$  can be separated using Eq. (9). We confirmed that the estimated  $\theta_{\text{e}}$  is within the accuracy in the sample angle control (see Supplementary Figure 4).

## DATA AVAILABILITY

The data that support the finding of this study are available from the corresponding author upon reasonable request.

---

- [1] Bychkov, Y. A. & Rashba, E. I. Properties of a 2D electron gas with lifted spectral degeneracy. *JETP Lett.* **39**, 78 (1984). [Pis'ma Zh. Eksp. Teor. Fiz. **39**, 66 (1984)].
- [2] Xiao, D., Liu, G.-B., Feng, W., Xu, X. & Yao, W. Coupled spin and valley physics in monolayers of MoS<sub>2</sub> and other group-VI dichalcogenides. *Phys. Rev. Lett.* **108**, 196802 (2012).
- [3] Sánchez, J. C. R. *et al.* Spin-to-charge conversion using Rashba coupling at the interface between non-magnetic materials. *Nat. Commun.* **4**, 2944 (2013).
- [4] Xu, X., Yao, W., Xiao, D. & Heinz, T. F. Spin and pseudospins in layered transition metal dichalcogenides. *Nat. Phys.* **10**, 343–350 (2014).
- [5] Manchon, A., Koo, H. C., Nitta, J., Frolov, S. M. & Duine, R. A. New perspectives for Rashba spin-orbit coupling. *Nat. Mater.* **14**, 871–882 (2015).
- [6] Gor'kov, L. P. & Rashba, E. I. Superconducting 2D system with lifted spin degeneracy: mixed singlet-triplet state. *Phys. Rev. Lett.* **87**, 037004 (2001).
- [7] Sekihara, T., Masutomi, R. & Okamoto, T. Two-dimensional superconducting state of monolayer Pb films grown on GaAs(110) in a strong parallel magnetic field. *Phys. Rev. Lett.* **111**, 057005 (2013).
- [8] Lu, J. M. *et al.* Evidence for two-dimensional Ising superconductivity in gated MoS<sub>2</sub>. *Science* **350**, 1353–1357 (2015).
- [9] Saito, Y. *et al.* Superconductivity protected by spin-valley locking in ion-gated MoS<sub>2</sub>. *Nat. Phys.* **12**, 144–149 (2016).
- [10] Nam, H. *et al.* Ultrathin two-dimensional superconductivity with strong spin-orbit coupling. *Proc. Natl. Acad. Sci.* **113**, 10513–10517 (2016).
- [11] Liu, Y. *et al.* Interface-induced Zeeman-protected superconductivity in ultrathin crystalline lead films. *Phys. Rev. X* **8**, 021002 (2018).
- [12] Bauer, E. & Sigrist, M. *Non-centrosymmetric superconductors: introduction and overview* (Springer, 2012).

- [13] Uchihashi, T. Two-dimensional superconductors with atomic-scale thickness. *Supercond. Sci. Technol.* **30**, 013002 (2016).
- [14] Chandrasekhar, B. S. A note on the maximum critical field of high-field superconductors. *Appl. Phys. Lett.* **1**, 7–8 (1962).
- [15] Clogston, A. M. Upper limit for the critical field in hard superconductors. *Physical Review Letters* **9**, 266–267 (1962).
- [16] Park, J. W. & Kang, M. H. Double-layer in structural model for the In/Si(111)- $\sqrt{7} \times \sqrt{3}$  surface. *Phys. Rev. Lett.* **109**, 166102 (2012).
- [17] Shirasawa, T., Yoshizawa, S., Takahashi, T. & Uchihashi, T. Structure determination of the Si(111)- $\sqrt{7} \times \sqrt{3}$ -In atomic-layer superconductor. *Phys. Rev. B* **99**, 055201 (2019).
- [18] Zhang, T. *et al.* Superconductivity in one-atomic-layer metal films grown on Si(111). *Nat. Phys.* **6**, 104–108 (2010).
- [19] Uchihashi, T., Mishra, P., Aono, M. & Nakayama, T. Macroscopic superconducting current through a silicon surface reconstruction with indium adatoms: Si(111)-( $\sqrt{7} \times \sqrt{3}$ )-In. *Phys. Rev. Lett.* **107**, 207001 (2011).
- [20] Gierz, I. *et al.* Silicon surface with giant spin splitting. *Phys. Rev. Lett.* **103**, 046803 (2009).
- [21] Sakamoto, K. *et al.* Abrupt rotation of the Rashba spin to the direction perpendicular to the surface. *Phys. Rev. Lett.* **102**, 096805 (2009).
- [22] Yaji, K. *et al.* Large Rashba spin splitting of a metallic surface-state band on a semiconductor surface. *Nat. Commun.* **1**, 1–5 (2010).
- [23] Matetskiy, A. V. *et al.* Two-dimensional superconductor with a giant Rashba effect: one-atom-layer TI-Pb compound on Si(111). *Phys. Rev. Lett.* **115**, 147003 (2015).
- [24] Rotenberg, E. *et al.* Indium  $\sqrt{7} \times \sqrt{3}$  on Si(111): a nearly free electron metal in two dimensions. *Phys. Rev. Lett.* **91**, 246404 (2003).
- [25] Yoshizawa, S. *et al.* Controlled modification of superconductivity in epitaxial atomic layer–organic molecule heterostructures. *Nano Lett.* **17**, 2287–2293 (2017).
- [26] Yoshizawa, S. *et al.* Imaging Josephson vortices on the surface superconductor Si(111)-( $\sqrt{7} \times \sqrt{3}$ )-In using a scanning tunneling microscope. *Phys. Rev. Lett.* **113**, 247004 (2014).
- [27] Kobayashi, T. *et al.* Orbital angular momentum induced spin polarization of 2D metallic bands. *Phys. Rev. Lett.* **125**, 176401 (2020).

- [28] Aslamasov, L. G. & Larkin, A. I. The influence of fluctuation pairing of electrons on the conductivity of normal metal. *Phys. Lett. A* **26**, 238–239 (1968).
- [29] Uchihashi, T., Mishra, P. & Nakayama, T. Resistive phase transition of the superconducting Si(111)-( $\sqrt{7} \times \sqrt{3}$ )-In surface. *Nanoscale Res. Lett.* **8**, 167 (2013).
- [30] Abrikosov, A. A. & Gor'kov, L. P. Spin-orbit interaction and the Knight shift in superconductors. *Sov. Phys. JETP* **15**, 752 (1962).
- [31] Maki, K. *Gapless Superconductivity*. in *Superconductivity: In Two Volumes* (ed. Parks, R. D.), chap. 18, 1035–1105 (Marcel Dekker, 1969).
- [32] Tinkham, M. *Introduction to superconductivity* (Dover, 2004).
- [33] Klemm, R. A., Luther, A. & Beasley, M. R. Theory of the upper critical field in layered superconductors. *Phys. Rev. B* **12**, 877–891 (1975).
- [34] Prober, D. E., Schwall, R. E. & Beasley, M. R. Upper critical fields and reduced dimensionality of the superconducting layered compounds. *Phys. Rev. B* **21**, 2717–2733 (1980).
- [35] Ziman, J. M. *Principles of the theory of solids: seond edition* (Cambridge University Press, 1979).
- [36] Maki, K. & Tsuneto, T. Pauli paramagnetism and superconducting state. *Prog. Theor. Phys.* **31**, 945–956 (1964).
- [37] Meservey, R. & Tedrow, P. M. Spin-orbit scattering in superconducting thin films. *Phys. Lett. A* **58**, 131–132 (1976).
- [38] Dimitrova, O. & Feigel'man, M. V. Theory of a two-dimensional superconductor with broken inversion symmetry. *Phys. Rev. B* **76**, 014522 (2007).
- [39] Samokhin, K. V. Upper critical field in noncentrosymmetric superconductors. *Phys. Rev. B* **78**, 224520 (2008).
- [40] Houzet, M. & Meyer, J. S. Quasiclassical theory of disordered Rashba superconductors. *Phys. Rev. B* **92**, 014509 (2015).
- [41] Frigeri, P. A., Agterberg, D. F., Koga, A. & Sigrist, M. Superconductivity without inversion symmetry: MnSi versus CePt<sub>3</sub>Si. *Phys. Rev. Lett.* **92**, 097001 (2004).
- [42] Sau, J. D., Lutchyn, R. M., Tewari, S. & Sarma, S. D. Generic new platform for topological quantum computation using semiconductor heterostructures. *Phys. Rev. Lett.* **104**, 040502 (2010).
- [43] Kitaev, A. Y. Unpaired Majorana fermions in quantum wires. *Phys.-Usp.* **44**, 131–136 (2001).
- [44] Dumitrescu, E., Zhang, C., Marinescu, D. C. & Tewari, S. Topological thermoelectric effects in spin-orbit coupled electron- and hole-doped semiconductors. *Phys. Rev. B* **85**, 245301 (2012).

- [45] Yaji, K. *et al.* High-resolution three-dimensional spin- and angle-resolved photoelectron spectrometer using vacuum ultraviolet laser light. *Rev. Sci. Instrum.* **87**, 053111 (2016).
- [46] Giannozzi, P. *et al.* QUANTUM ESPRESSO: a modular and open-source software project for quantum simulations of materials. *J. Phys. Condens. Matter* **21**, 395502 (2009).
- [47] Ozaki, T. Variationally optimized atomic orbitals for large-scale electronic structures. *Phys. Rev. B* **67**, 155108 (2003).
- [48] Ozaki, T. *et al.* OpenMX: open source package for Material eXplorer. <http://www.openmx-square.org/> (2019).

## ACKNOWLEDGEMENTS

We thank Y. Higashi, S. Ichinokura and T. Shishidou for helpful discussions. We also thank K. Kuroda and A. Harasawa for their technical supports during the ARPES experiments. This work was supported financially by JSPS KAKENHI (Grant Numbers 18H01876, 16K17727, 25247053, 19H02592, 19H00651, 18K03484, 17H05211, and 17H05461), by Advanced Technology Institute (ATI) Research Grants 2017, and by World Premier International Research Center (WPI) Initiative on Materials Nanoarchitectonics, MEXT, Japan.

## AUTHOR CONTRIBUTIONS

S.Y. and T.U. conceived the experiment and wrote the manuscript. S.Y, K. Yokota, and T.U. carried out the electron transport experiments. S.Y. analysed the transport data and performed the DFT calculations. T.K., Y.N., K. Yaji, and K.S. measured the ARPES data with supports from F.K. and S.S. All the authors discussed the results and contributed to finalising the manuscript.

## COMPETING INTERESTS

The authors declare no competing interests.



Sample	miscut	$R_n$	$T_{c0}$	$B_{\text{Pauli}}$	$\xi$	$c_{O\perp}$	$c_{O\parallel}$	$c_P$	$\theta_c$	$\tau_s$	$\tau_{el}$
	(deg.)	( $\Omega$ )	(K)	(T)	(nm)	(meV·T <sup>-1</sup> )	( $\mu$ eV·T <sup>-2</sup> )	( $\mu$ eV·T <sup>-2</sup> )	(deg.)	(fs)	(fs)
Flat#1	0	35.9	3.14	5.83	41.3 (2.9)	1.67 (0.09)	0.086 (0.005)	0.66 (0.09)	0.07 (0.02)	86 (12)	71.7
Flat#2	0	48.3	3.14	5.83	41.4 (2.7)	1.68 (0.08)	0.086 (0.004)	0.39 (0.11)	0.12 (0.02)	52 (14)	53.3
Flat#3	0	53.2	3.11	5.78	42.9 (1.9)	1.85 (0.16)	0.095 (0.008)	0.25 (0.14)	0.21 (0.03)	33 (18)	44.9
Vicinal#1	0.5	90.0	2.99	5.55	29.2 (0.9)	0.83 (0.02)	0.042 (0.001)	0.53 (0.09)	0.08 (0.03)	69 (12)	28.6
Vicinal#2	0.5	65.7	3.04	5.64	30.3 (0.9)	0.90 (0.02)	0.046 (0.001)	0.53 (0.09)	0.04 (0.03)	70 (12)	39.2
Vicinal#3	1.1	82.1	2.97	5.52	31.9 (0.6)	0.99 (0.04)	0.051 (0.002)	0.44 (0.09)	0.06 (0.03)	57 (12)	31.4

**Table 1 | List of parameters obtained for the six samples.**  $\xi$  is the Ginzburg-Landau coherence length estimated from the data in out-of-plane magnetic fields (See Supplementary Note 2). The values in the parentheses are the estimates of errors propagated from the accuracy of the calibration curve for magnetoresistance of the temperature sensor (0.005 K for  $B \leq 5$  T and 0.04 K for  $B \geq 5$  T) and the hysteresis of the superconducting magnet (0.004 T).

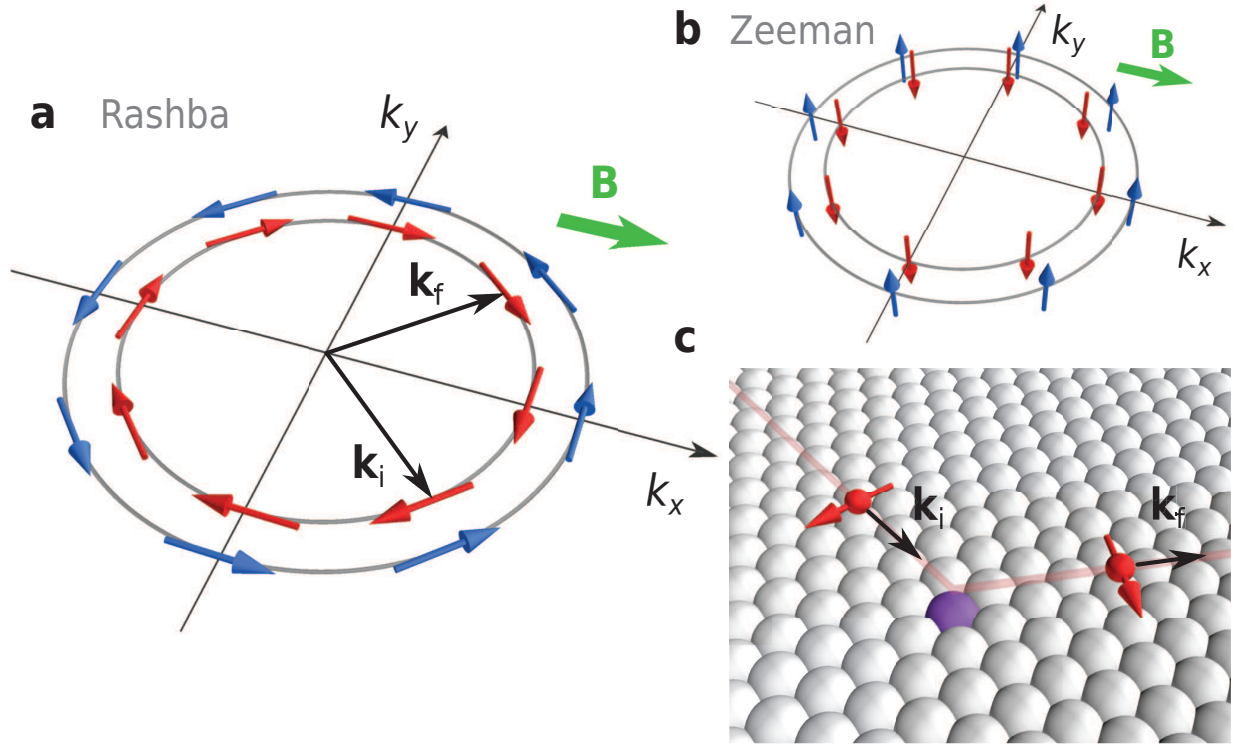


**Figure 1 | Schematic illustration of dynamic spin-momentum locking.** (a) Fermi surfaces in the presence of Rashba-type SOC. The spins are polarized in the in-plane directions and locked to the momentum. The split Fermi surfaces are characterized by spin textures with opposite helicities. (b) Fermi surfaces in the presence of Zeeman-type SOC. The spins are oriented in the out-of-plane directions. The green arrows in (a) and (b) indicate a magnetic field applied in the in-plane direction. (c) When an electron at the initial state  $\mathbf{k}_i$  is elastically scattered to  $\mathbf{k}_f$  by a non-magnetic scattering centre (depicted by a purple ball), its spin is forced to rotate.

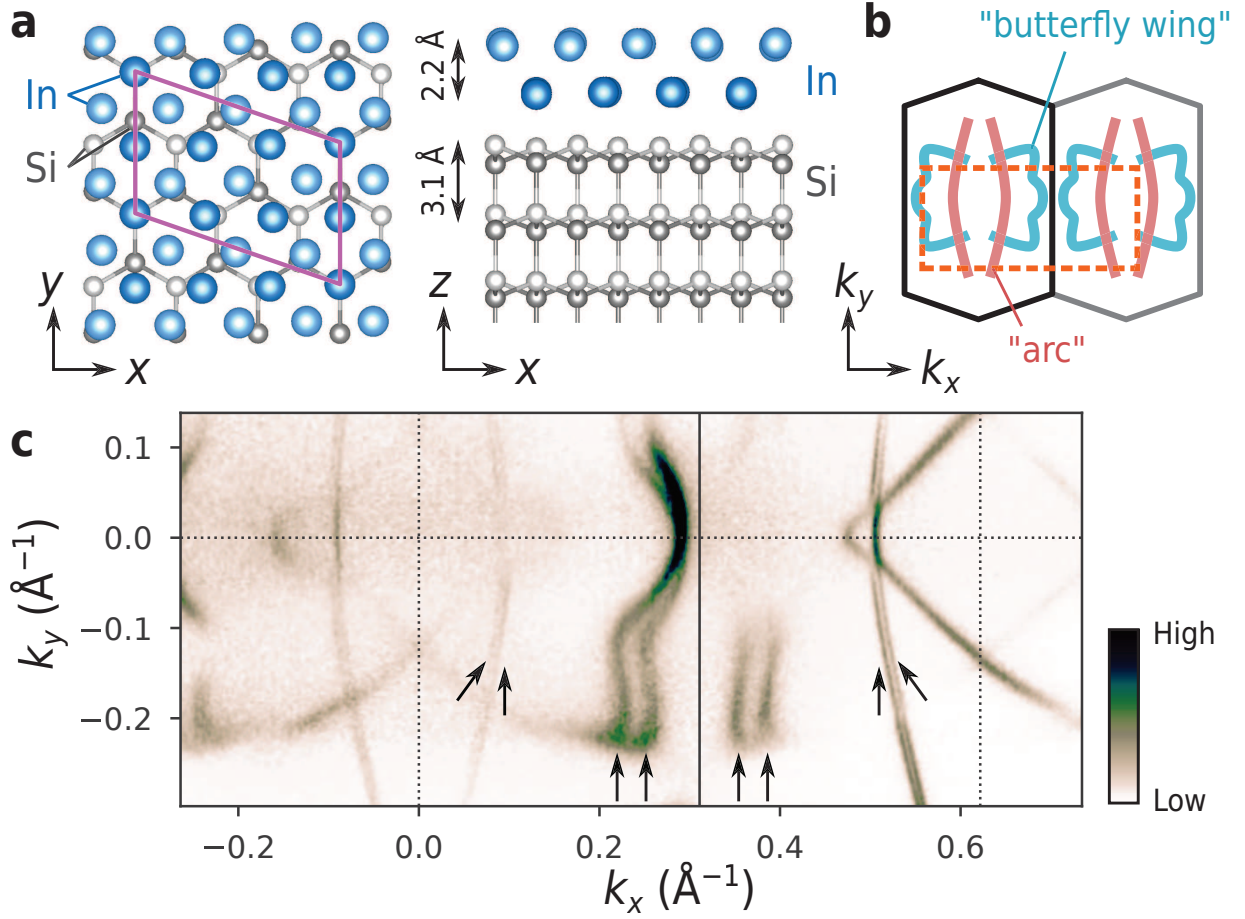


**Figure 2 | Crystal structure and experimentally-observed Fermi surface.** (a) Top view (left) and side view (right) of the crystal structure of  $\sqrt{7} \times \sqrt{3}$ -In. The  $x$ ,  $y$ , and  $z$  axes are defined to be  $[1\bar{1}0]$ ,  $[11\bar{2}]$ , and  $[111]$  directions, respectively. (b) Schematic of the 1st and 2nd Brillouin zones. The dashed box represents the area of the photoelectron intensity map in (c). The characteristic arc feature and butterfly-wing feature of the Fermi surface are depicted. (c) Photoelectron intensity map at  $E_F$ . The arrows indicate the portions of the Fermi surface with a clear splitting.

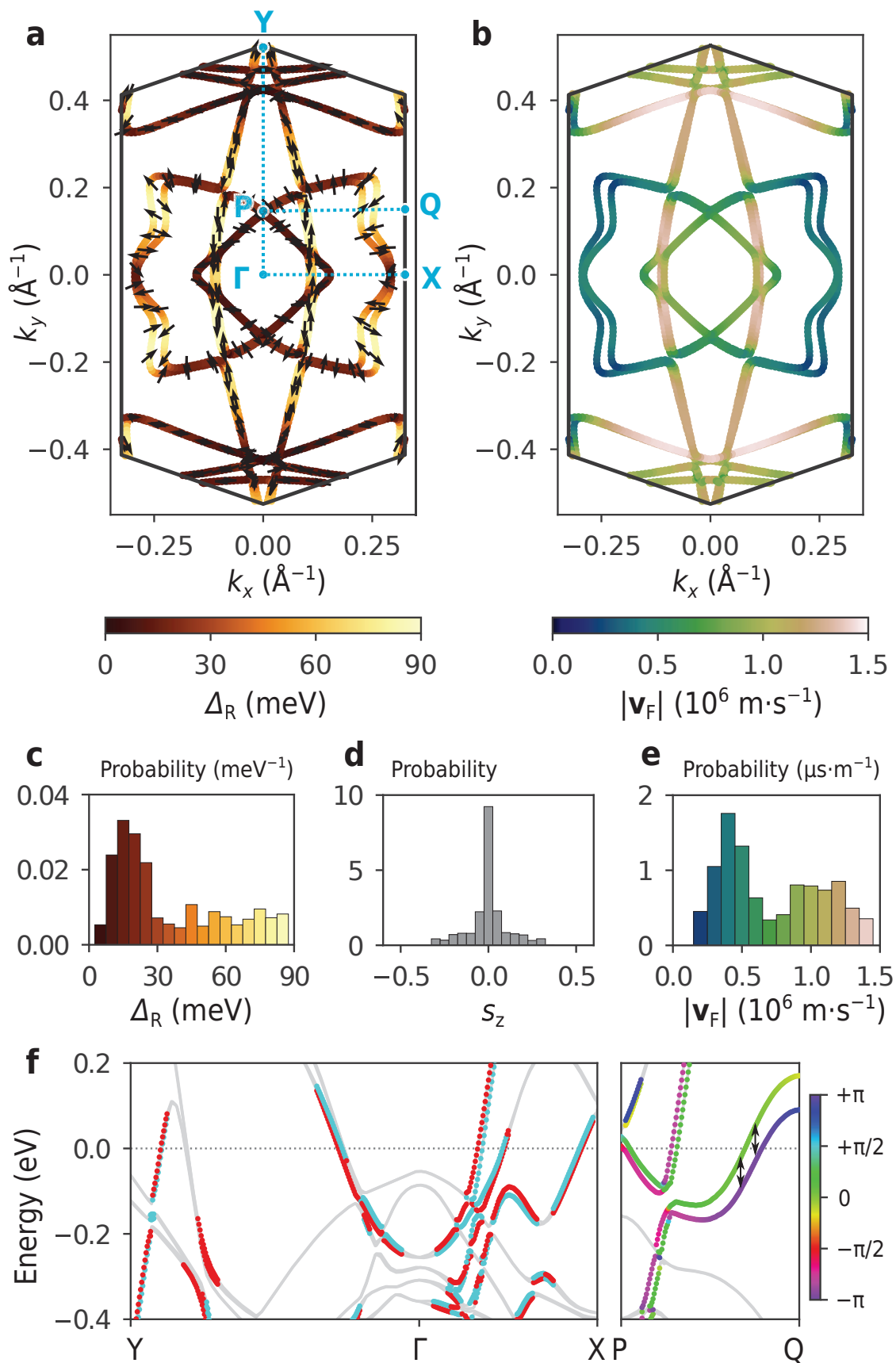


**Figure 3 | Computed spin-split Fermi surface and Fermi velocity.** (a) Fermi surface obtained from the DFT calculation. The colour indicates the magnitude of band splitting  $\Delta_R$ . Here,  $\Delta_R$  is defined at each point on the Fermi surface as the energy difference from the partner band, as depicted by the double-headed arrows in (f). The small arrows indicate the orientation of the spins. (b) Fermi velocity  $|\mathbf{v}_F|$  computed from the band dispersion. (c)-(e) Histograms of  $\Delta_R$  (c), the z component of the spin,  $s_z$ , (d), and  $|\mathbf{v}_F|$  (e) measured on the Fermi surface. These histograms reflect the weighting factor to the density of states given by  $dl/|\mathbf{v}_F|$ , where  $dl$  is the line segment on the Fermi surface. (c) and (e) share the same colour scales as (a) and (b), respectively. (f) Energy bands along Y- $\Gamma$ -X and P-Q. The vertical axis shows the energy measured from the Fermi level. The colour indicates the relative direction of spin with respect to momentum; red and cyan correspond to the clockwise and counterclockwise helicities. For clarity, the states with  $\Delta_R < 10$  meV are coloured in grey.

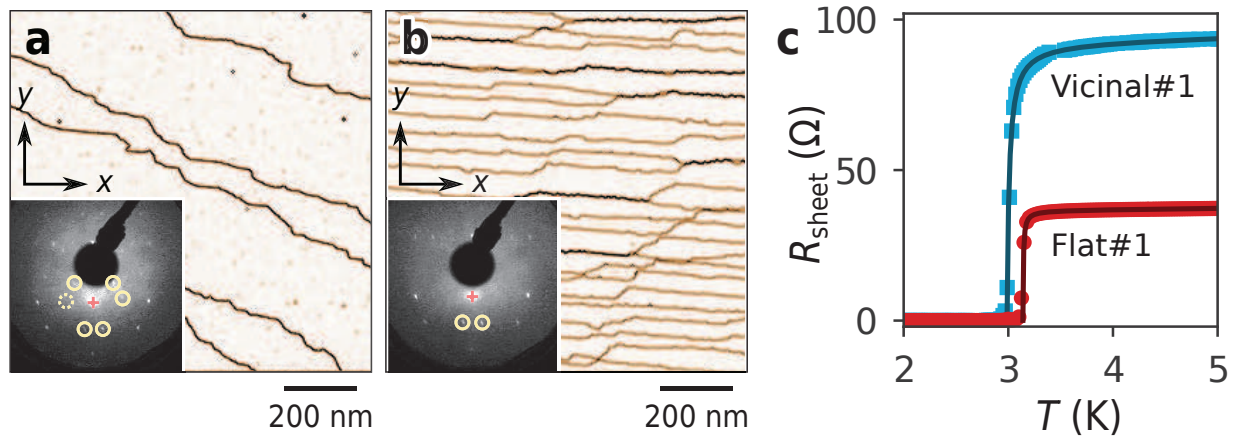


**Figure 4 | Characterisation of samples for electron transport measurements.** (a) and (b) STM images of Flat#1 and Vicinal#1, respectively. The derivative (gradient) of the topographic data are displayed for highlighting the locations of atomic steps. The insets are the corresponding LEED patterns taken at a 94 eV beam energy. The circles indicate the peaks reflecting the  $\sqrt{7} \times \sqrt{3}$  periodicity. The plus symbol indicates (0,0). (c) Resistance curves of Flat#1 and Vicinal#1 measured at zero magnetic field. The solid curves are the fitting by an empirical formula (See Supplementary Note 1).

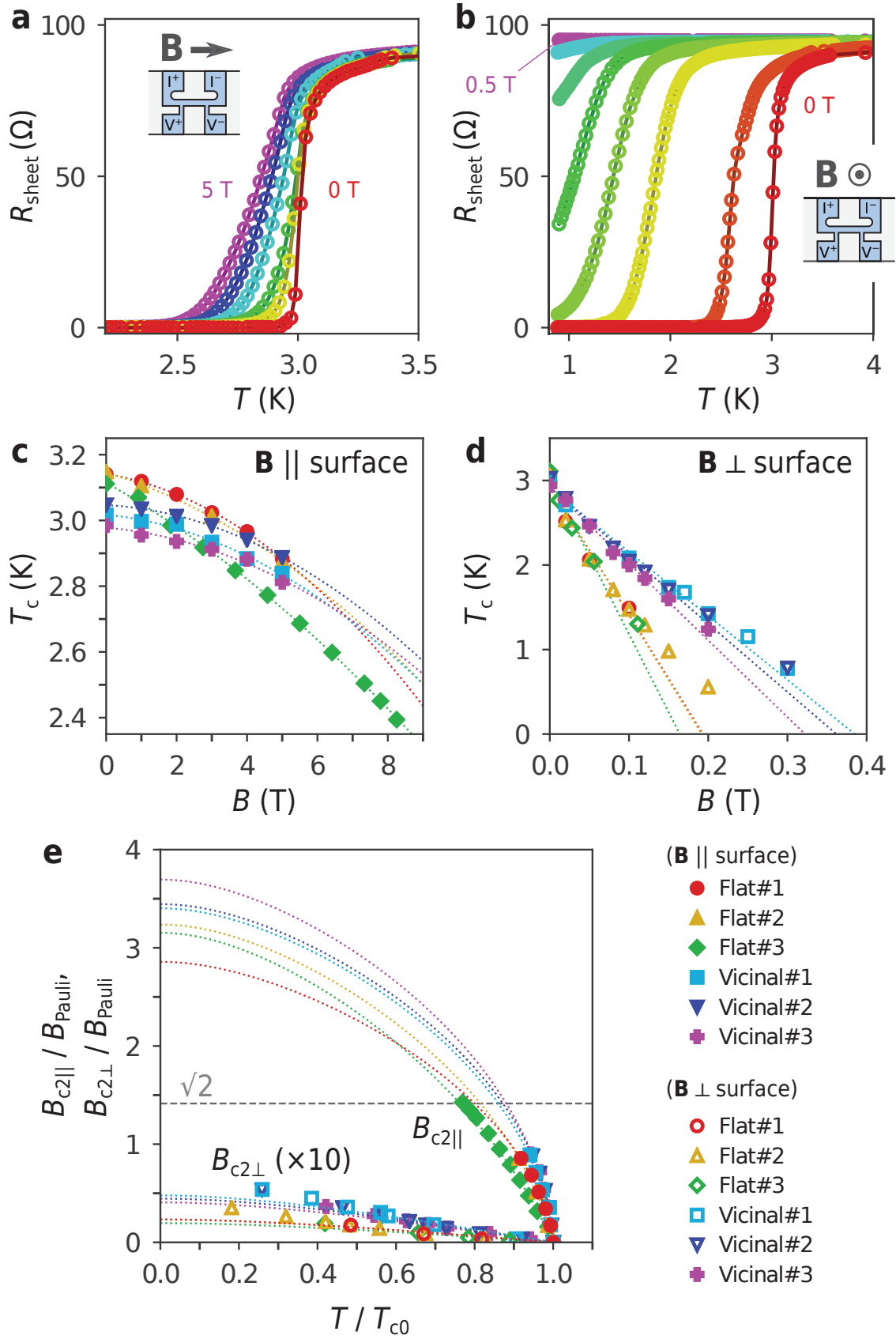


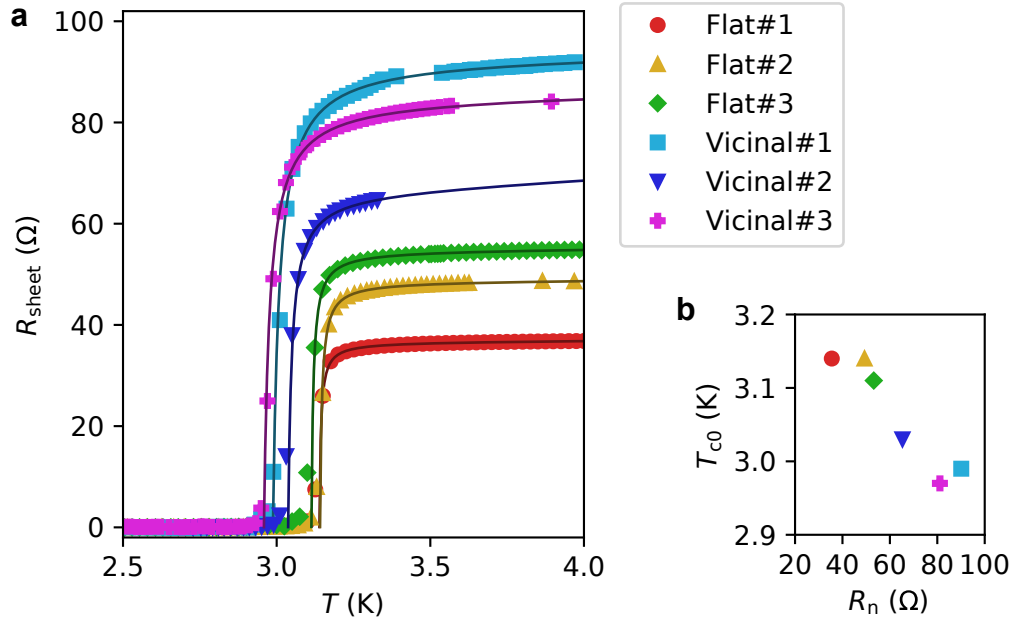
**Figure 5 | Superconducting properties in in-plane and out-of-plane magnetic fields.** (a) Resistance curves of Vicinal#1 in in-plane magnetic fields of  $B = 0, 1, 2, 3, 4$  and  $5$  T. (b) Resistance curves of Vicinal#1 in out-of-plane magnetic fields of  $B = 0, 0.02, 0.1, 0.15, 0.2, 0.25, 0.3$  and  $0.5$  T. The insets of (a) and (b) show the directions of the magnetic fields with respect to the samples. The samples were patterned in a shape suitable for four-terminal measurements, as represented by areas coloured in light blue.  $I^{+(-)}$  and  $V^{+(-)}$  are the current and voltage terminals, respectively. (c) Field dependence of  $T_c$  in in-plane magnetic fields. (d) Field dependence of  $T_c$  in out-of-plane magnetic fields. The dotted curves in (c) and (d) are the quadratic and linear functions fitted to the data. (e) Comparison of  $B_{c2\parallel}$  and  $B_{c2\perp}$ . For clarity,  $B_{c2\perp}$  is scaled by a factor of 10. The dotted curves are the universal function Eq. (1) plotted with parameters determined from the fitting analyses. The dashed horizontal line indicates the enhancement factor  $\sqrt{2}$  for static locking effect of Rashba-type SOC. The relatively large variation in the fitting curves for  $B_{c2\parallel}$  originates mainly from the angular error of the sample orientation denoted by  $\theta_e$  in the main text.



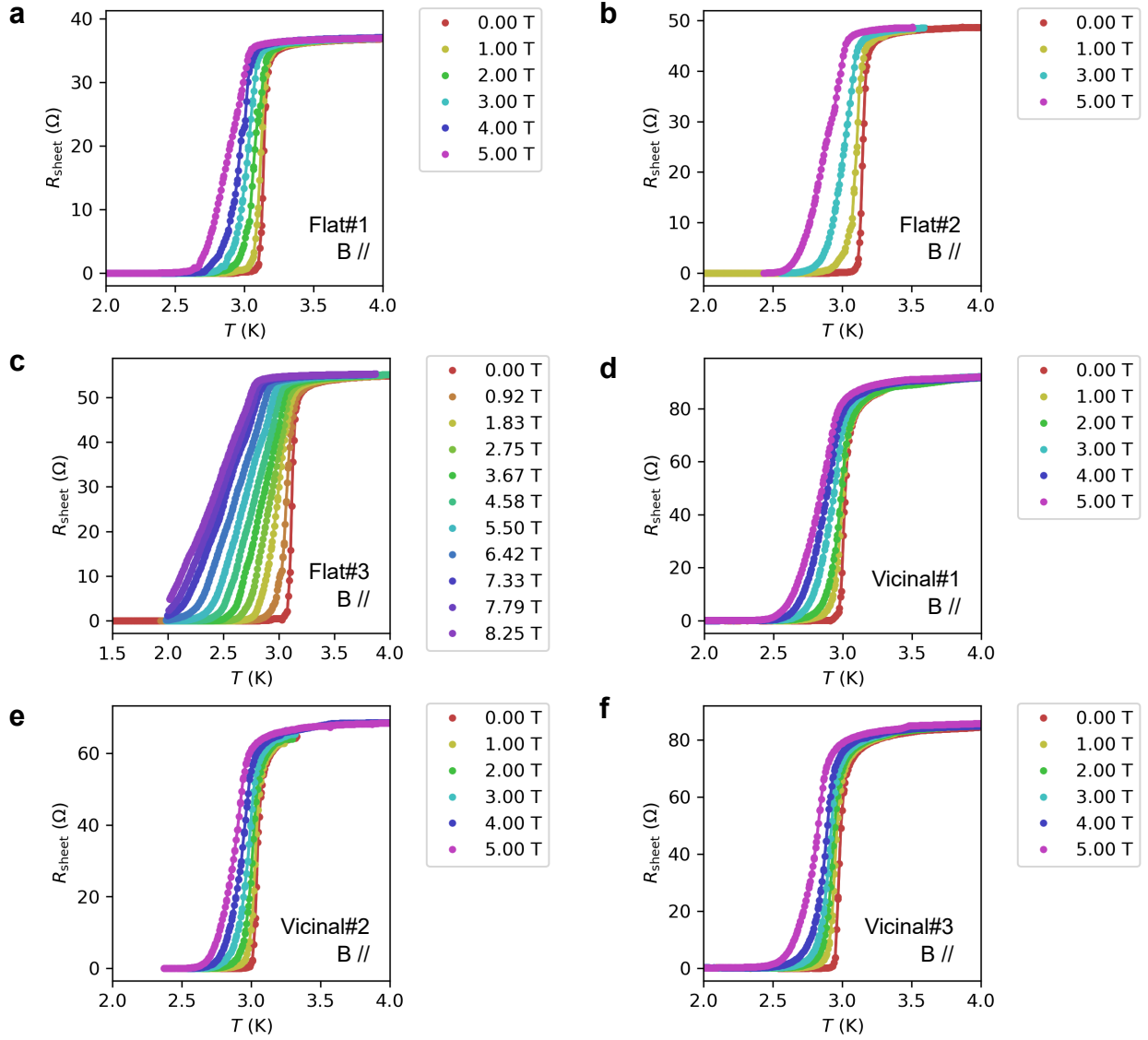
Supplementary Information for

# Atomic-layer Rashba-type superconductor protected by dynamic spin-momentum locking

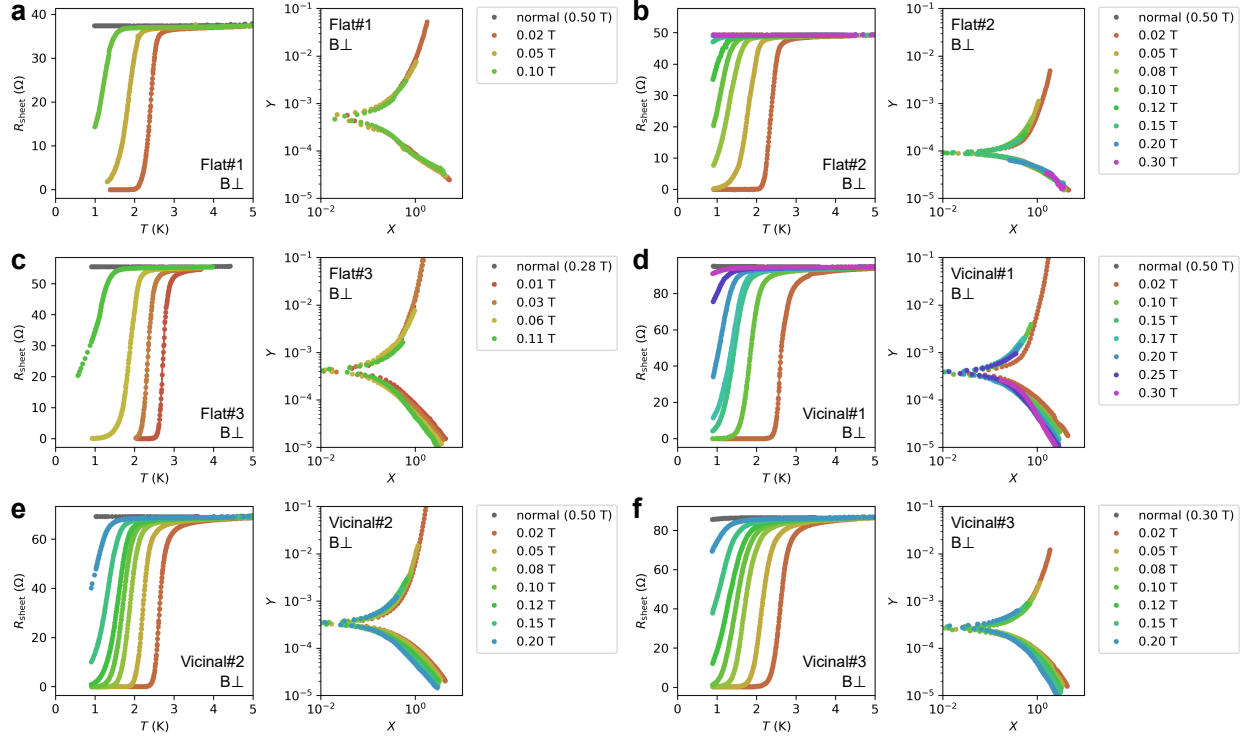
Shunsuke Yoshizawa, Takahiro Kobayashi, Yoshitaka Nakata, Koichiro Yaji, Kenta Yokota,  
Fumio Komori, Shik Shin, Kazuyuki Sakamoto, and Takashi Uchihashi



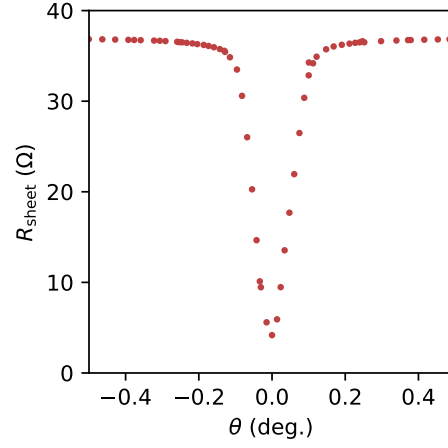
**Supplementary Figure 1 | Determination of zero-field critical temperature.** (a) Resistance curves of the six samples (Flat#1, Flat#2, Flat#3, Vicinal#1, Vicinal#2, and Vicinal#3) measured in zero magnetic fields are plotted. The solid curves show the results of the fitting. (b) Zero-field critical temperature ( $T_{c0}$ ) plotted as a function of normal-state resistance ( $R_n$ ).



**Supplementary Figure 2 | Superconducting transition in in-plane magnetic fields.** (a-f) Resistance curves of the six samples (Flat#1, Flat#2, Flat#3, Vicinal#1, Vicinal#2, and Vicinal#3) in in-plane magnetic fields.

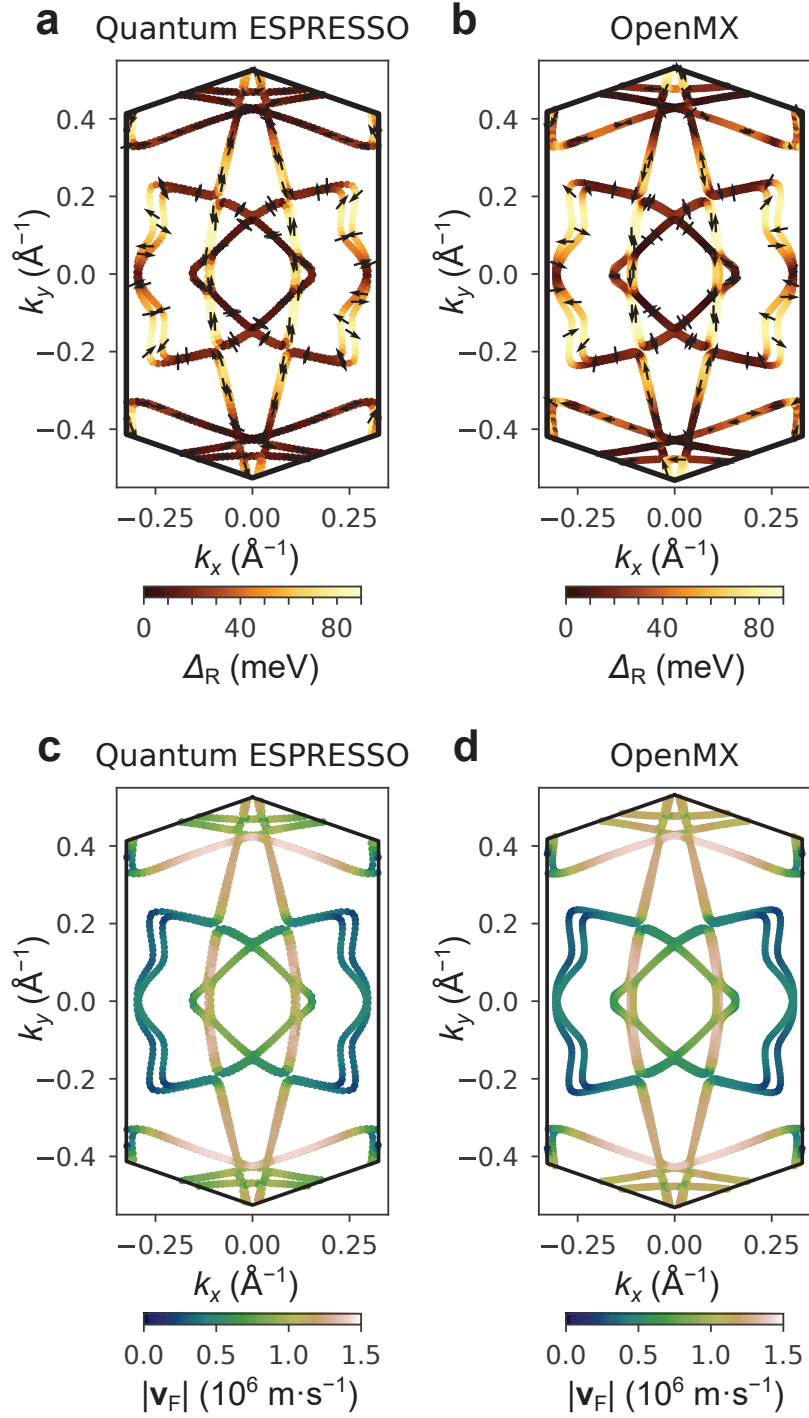


**Supplementary Figure 3 | Superconducting transition in out-of-plane magnetic fields.** (a-f) Resistance curves (left) and the plots of the Ullah-Dorsey scaling analysis<sup>1,2</sup> (right) of the six samples (Flat#1, Flat#2, Flat#3, Vicinal#1, Vicinal#2, and Vicinal#3) in out-of-plane magnetic fields. The axes of the scaling plot are  $X = |T - T_c|(BT)^{-1/2}$  and  $Y = (B/T)^{1/2}$ .

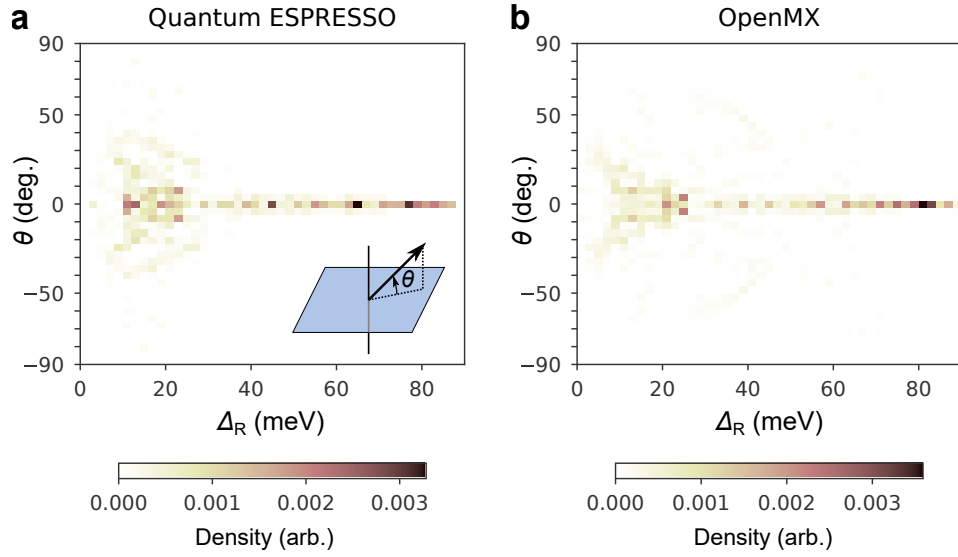


**Supplementary Figure 4 | Accuracy in the sample alignment for in-plane magnetic fields.**

The plot shows the typical angular dependence of the sheet resistance near the critical temperature. Here,  $R_{\text{sheet}}$  was measured at  $T = 2.8$  K in  $B = 5$  T. The sample angle  $\theta$  was determined from the signal of the Hall sensor attached on the rotatable sample stage. The parallel sample configuration was found from the minimum of the curve by changing  $\theta$  at an accuracy of  $\sim 0.05^\circ$  for each sample.



**Supplementary Figure 5 | Comparison of calculations using Quantum ESPRESSO and OpenMX.** (a,b) Band splitting and spin polarisation direction of  $\sqrt{7} \times \sqrt{3}$ -In calculated with (a) Quantum ESPRESSO and (b) OpenMX. (c,d) Fermi velocity calculated with (c) Quantum ESPRESSO and (d) OpenMX.



**Supplementary Figure 6 | Spin polarization direction on the Fermi surface.** Spin orientation relative to the in-plane direction is displayed as a function of energy splitting. The results are obtained using (a) Quantum ESPRESSO and (b) OpenMX.  $\theta = 0^\circ$  corresponds to the in-plane direction while  $\theta = 90^\circ$  the out-of-plane direction (see the inset of a).

### Supplementary Note 1 | Fitting analysis of zero-field data

The zero-field critical temperature  $T_{c0}$  and the normal-state residual resistance  $R_n$  were determined by fitting a function of the form<sup>3</sup>,

$$\frac{1}{R_{\text{sheet}}} = \frac{1}{R_n + cT^a} + \frac{1}{R_0} \frac{T}{T - T_{c0}} \quad (1)$$

to the resistance curves (Supplementary Figure 1a) for  $T > T_{c0}$ . Here, the first term represents normal-state conductance;  $a$  and  $c$  represent phonon contribution; the second term represents the fluctuation effect characteristic to 2D superconductors<sup>4</sup>; and  $R_0$  is the temperature-independent parameter. As presented in Supplementary Figure 1b,  $T_{c0}$  is found to be a monotonic decreasing function of  $R_n$ , being order-of-magnitude consistent with the theoretical behaviour of superconducting films containing non-magnetic impurities<sup>5</sup>. This consistency suggests that the atomic steps work as non-magnetic scatterers in the present condition, while it serves as Josephson junctions when the supercurrent density approaches the critical value<sup>6,7</sup>. The weak dependence of  $T_{c0}$  on  $R_n$  indicates that the s-wave pairing is dominant.

### Supplementary Note 2 | Analysis of pair-breaking mechanism in out-of-plane fields

The linear B dependence of  $T_c$  observed for out-of-plane fields (Fig. 5d, which was obtained from the scaling analysis shown in Supplementary Figure 3) is consistent with the Ginzburg-Landau (GL) theory<sup>8</sup>. We estimate the extrapolated value of GL coherence length,  $\xi$ , by fitting the following function valid near  $T_{c0}$ ,

$$B = \frac{\Phi_0}{2\pi\xi^2} \left(1 - \frac{T_c}{T_{c0}}\right) \quad (2)$$

where  $\Phi_0 = h/(2e)$  is the flux quantum. As presented in Table 1,  $\xi$  ranges between 29-43 nm, which are consistent with the radii of vortices (36-47 nm) reported in STM studies<sup>7</sup>. This indicates that the perpendicular critical field is limited by the orbital pair-breaking effect, i.e., penetration of vortices.

### Supplementary Note 3 | The influence of the static effect of the Rashba-type SOC

The static effect of the spin-momentum locking due to the Rashba-type SOC is known to enhance the in-plane critical field  $B_{c2\parallel}$  by a factor of 2 from the Pauli limit. This effect is likely to be



weakened by electron scattering and mixing between different spin states. Since we do not know the degree of such an effect, we assume the worst case and estimate the upper limit of error in  $\tau_s$  in the following.

In the absence of spin-orbit coupling, the  $B$  dependence of  $T_c$  near  $T_{c0}$  is given by

$$1 - \frac{T_c}{T_{c0}} = \frac{7\zeta(3)}{4\pi^2} \cdot \frac{(\mu_B B)^2}{(k_B T_{c0})^2}. \quad (3)$$

With the static spin-momentum locking due to Rashba SOC, the expression changes to<sup>9</sup>

$$1 - \frac{T_c}{T_{c0}} = \frac{1}{2} \cdot \frac{7\zeta(3)}{4\pi^2} \cdot \frac{(\mu_B B)^2}{(k_B T_{c0})^2}. \quad (4)$$

Here the addition of the factor 1/2 in Eq. (4) means that  $B$  is replaced with an effective magnetic field  $B_{\text{eff}} = (1/\sqrt{2})B$  in Eq. (3). This is the origin of the enhancement of  $B_{c2}$  by a factor of  $\sqrt{2}$  due to the static locking effect of Rashba SOC. The effect of non-magnetic disorder on a Rashba superconductor can be estimated using this effective magnetic field. By substituting  $B$  with  $B_{\text{eff}} = (1/\sqrt{2})B$  in the following equations (taken from Eqs. (3) and (6) in the main text; only the paramagnetic contribution is considered here),

$$\alpha(B) = c_P B^2 \quad (5)$$

and

$$c_P = \frac{3\tau_s \mu_B^2}{2\hbar}. \quad (6)$$

We see that  $\tau_s$  value is doubled for the same experimental data  $\alpha(B)$ . With the  $\tau_s$  values obtained previously (see Table 1) in the manuscript, we can estimate that the lower limit of  $\tau_{\text{el}}/\tau_s$  is 0.25-0.5. These values are still much higher than 1/60-1/1000 for thin In films, which is due to the atomistic spin-orbit scattering mechanism. Therefore, the result is not attributable only to the conventional mechanism, and our conclusion remains the same.

#### **Supplementary Note 4 | The role of the Zeeman-type SOC in the $B_{c2}$ enhancement**

The distribution of spin polarisation direction was obtained from our DFT results (Supplementary Figure 6a). It clearly shows that the spins align in the in-plane directions for the most of energy regions. This means that Rashba SOC is dominant over Zeeman SOC mostly. The spins tend to tilt toward the out-of-plane direction below 30 meV, but the off-angle is about 45° at most.

Namely, there is no region where Zeeman SOC is dominant. This result was also reproduced by the calculations using OpenMX (Supplementary Figure 6b).

This non-dominant Zeeman SOC confined to small area of the Fermi surface can barely enhance  $B_{c2}$ . This is because enhancement factor is determined by an average over the whole Fermi surface. The critical temperature in the presence of magnetic field  $B$ ,  $T_c(B)$ , is given by the following equations<sup>10,11</sup>,

$$\ln\left(\frac{T_c(\mathbf{B})}{T_{c0}}\right) = 2 \left\langle |\psi(\mathbf{k})|^2 f\left(\frac{\mathbf{g}(\mathbf{k}) \cdot \mathbf{B}}{\pi T_c |\mathbf{g}(\mathbf{k})|}\right) \right\rangle_{\mathbf{k}} \quad (7)$$

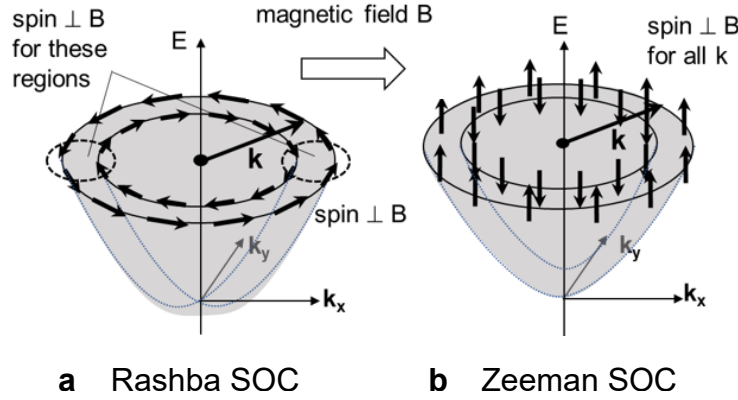
and

$$f(x) = \text{Re} \sum_{n=1}^{\infty} \left( \frac{1}{2n-1+ix} - \frac{1}{2n-1} \right), \quad (8)$$

where  $T_{c0} \equiv T_c(\mathbf{B} = 0)$ ,  $\mathbf{k}$  is the wavevector on the Fermi surface,  $\psi(\mathbf{k})$  is the spin-singlet gap function,  $\mathbf{g}(\mathbf{k})$  is a vector determining the spin polarisation at each  $\mathbf{k}$ , and  $\langle \dots \rangle_{\mathbf{k}}$  denotes taking an average over the Fermi surface.  $B_{c2}$  is given by  $\mathbf{B}$  that satisfies  $T_c(\mathbf{B}) = 0$ . For example, when magnetic field is applied parallel to the Rashba-split Fermi surface, spins in some regions point nearly perpendicular to the field (see the figure (a) below). This is analogous to the Zeeman SOC case (see the figure (b) below), but the enhancement factor is limited to 2 because of the averaging over the whole Fermi surface. This clearly shows that, even if Zeeman SOC coexists in the present system and tilts some of the spins toward the out-of-plane direction, its effect is limited.

If the dynamics of spins is considered, the effect of the Zeeman-type SOC can be suppressed even more. Since our system is characterised by dominant Rashba-type SOC, the polarisation axis of the spins strongly depends on momentum. This means that electron scattering between different momenta effectively induce a spin flipping and therefore out-of-plane spin component is not conserved through elastic scattering. We note that a different situation takes place for an ultrathin layer of TMDC with Zeeman-type SOC<sup>12,13</sup>. Here, since all the spins around one of the valleys are polarised in the same out-of-plane direction, dominant intravalley scatterings cannot cause spin flipping<sup>14</sup>. By contrast, this mechanism does not apply to our Rashba-type SOC case because of the presence of frequent spin flipping.

Base on all these facts, we conclude that strong enhancement of  $B_{c2}$  due to Zeeman SOC is extremely unlikely in the present system.



Schematic illustration of the Fermi surface splitting due to (a) Rashba SOC and (b) Zeeman SOC.

### Supplementary Note 5 | Computational condition for OpenMX

We performed DFT calculations using OpenMX to confirm the reproducibility of the computational results. OpenMX is based on the optimised pseudo-atomic orbitals (PAO)<sup>15</sup>, and we selected from the “Precise” sets from the PAO database (2019) in the OpenMX website<sup>16</sup>. We chose LSDA-CA<sup>17,18</sup> for the exchange-correlation functional. The crystal structure of  $\sqrt{7} \times \sqrt{3}$ -In was modeled by a repeated slab consisting of an In bilayer, nine Si bilayers, a H layer for termination, and a vacuum region of 4.5 nm. We set the cutoff energy to 300 Ry and the  $k$ -point mesh to  $6 \times 8 \times 1$ . The geometry optimisation was performed without SOC until the maximum force on each atom became less than  $1 \times 10^{-5}$  Hartree·Bohr<sup>-1</sup>. The band calculation was carried out using the optimised structure by including SOC. The spin texture was analysed by using kSpin code<sup>19</sup>.

### Supplementary References

1. Ullah, S. & Dorsey, A. T. Effect of fluctuations on the transport properties of type-II superconductors in a magnetic field. *Phys. Rev. B* **44**, 262–273 (1991).
2. Saito, Y., Nojima, T. & Iwasa, Y. Quantum phase transitions in highly crystalline two-dimensional superconductors. *Nat. Commun.* **9**, 778 (2018).
3. Uchihashi, T., Mishra, P. & Nakayama, T. Resistive phase transition of the superconducting Si(111)-( $\sqrt{7} \times \sqrt{3}$ )-In surface. *Nanoscale Res. Lett.* **8**, 167 (2013).
4. Aslamasov, L. G. & Larkin, A. I. The influence of fluctuation pairing of electrons on the conductivity of normal metal. *Phys. Lett. A* **26**, 238–239 (1968).

5. Finkel'stein, A. M. Suppression of superconductivity in homogeneously disordered systems. *Physica B: Condensed Matter* **197**, 636–648 (1994).
6. Uchihashi, T., Mishra, P., Aono, M. & Nakayama, T. Macroscopic superconducting current through a silicon surface reconstruction with indium adatoms: Si(111)-( $\sqrt{7} \times \sqrt{3}$ )-In. *Phys. Rev. Lett.* **107**, 207001 (2011).
7. Yoshizawa, S. *et al.* Imaging Josephson vortices on the surface superconductor Si(111)-( $\sqrt{7} \times \sqrt{3}$ )-In using a scanning tunneling microscope. *Phys. Rev. Lett.* **113**, 247004 (2014).
8. Tinkham, M. *Introduction to superconductivity* (Dover, 2004).
9. Barzykin, V. & Gor'kov, L. P. Inhomogeneous stripe phase revisited for surface superconductivity. *Phys. Rev. Lett.* **89**, 227002 (2002).
10. Frigeri, P. A., Agterberg, D. F., Koga, A. & Sigrist, M. Superconductivity without inversion symmetry: MnSi versus CePt<sub>3</sub>Si. *Phys. Rev. Lett.* **92**, 097001 (2004).
11. Smidman, M., Salamon, M. B., Yuan, H. Q. & Agterberg, D. F. Superconductivity and spin–orbit coupling in non-centrosymmetric materials: a review. *Rep. Prog. Phys.* **80**, 036501 (2017).
12. Lu, J. M. *et al.* Evidence for two-dimensional Ising superconductivity in gated MoS<sub>2</sub>. *Science* **350**, 1353–1357 (2015).
13. Saito, Y. *et al.* Superconductivity protected by spin-valley locking in ion-gated MoS<sub>2</sub>. *Nat. Phys.* **12**, 144–149 (2016).
14. Ilić, S., Meyer, J. S. & Houzet, M. Enhancement of the upper critical field in disordered transition metal dichalcogenide monolayers. *Phys. Rev. Lett.* **119**, 117001 (2017).
15. Ozaki, T. Variationally optimized atomic orbitals for large-scale electronic structures. *Phys. Rev. B* **67**, 155108 (2003).
16. Ozaki, T. *et al.* OpenMX: open source package for Material eXplorer. <http://www.openmx-square.org/> (2019).
17. Ceperley, D. M. & Alder, B. J. Ground state of the electron gas by a stochastic method. *Phys. Rev. Lett.* **45**, 566–569 (1980).
18. Perdew, J. P. & Zunger, A. Self-interaction correction to density-functional approximations for many-electron systems. *Phys. Rev. B* **23**, 5048–5079 (1981).
19. Kotaka, H., Ishii, F. & Saito, M. Rashba effect on the structure of the Bi one-bilayer film: fully relativistic first-principles calculation. *Jpn. J. Appl. Phys.* **52**, 035204 (2013).